Three-dimensional analysis of the collision process of a bead on a granular packing

Madani Ammi, Luc Oger, Djaoued Beladjine, and Alexandre Valance
Institut de Physique de Rennes, Université de Rennes 1, UMR UR1-CNRS 6251, F-35042 Rennes Cedex, France
(Received 30 September 2008; revised manuscript received 8 December 2008; published 18 February 2009)

We present results of the collision process of a bead onto a static granular packing. We provide, in particular, a three-dimensional (3D) extensive characterization of this process from a model experiment that allows us to propel a spherical bead onto a granular packing with a well-controlled velocity and impact angle. A collision typically produces a high-energy particle (rebound particle) and several low-energy grains (ejected particles). The collision process is recorded by means of two fast video cameras. The sequence of images from both cameras are then analyzed via image processing and the trajectories of all particles are reconstructed in 3D space. We show that the incident particle does not remain in the vertical incident plane after the rebound and that the deviation angle increases with increasing impact angle. Concerning the ejected particles, we demonstrated that the ejection angle (measured with respect to the horizontal plane) is surprisingly independent of both the impact angle and velocity of the incident particle, and is very close to 60°. The horizontal component of the ejection speed of the splashed particles is found to be weakly dependent on the incident speed and impact angle, and is relatively isotropic (no particular horizontal direction is favored). This last feature suggests that the bead packing acts as a perfect diffusive medium with respect to energy propagation.

DOI: 10.1103/PhysRevE.79.021305 PACS number(s): 45.70.−n, 62.20.−x, 81.05.Rm

I. INTRODUCTION

Saltation in which sand grains are propelled by the wind along the surface in short hops, is the primary mode of blown sand movement [1]. The saltating grains are very energetic and when they impact a sandy surface, they rebound and also eject other particles from the sand bed. The ejected grains (called reptating grains) are weakly energetic but as they are numerous, they contribute to the augmentation of the sand flux and some of them are accelerated by the wind and become saltating grains. The understanding of the impact process, also termed "splash," is crucial to model the aeolian sand transport.

A large number of studies have been devoted to the splash process in aeolian sand transport. Wind tunnel experiments were conducted to reproduce the aeolian sand transport and analyze the behavior of the saltating grains [2–5]. These experiments evidenced that the saltating grain impacts the bed at grazing angles in the range of 8° to 15° and rebounds with a smaller velocity, usually at a greater angle (between 20° to 40°). Collision models, consisting of shooting a particle on a granular bed with a well-controlled speed and impact angle, either experimental [6–9] or numerical [10–12], were developed in order to gain more information about the ejected particles. Experimental collision models gave a rather complete picture of the splash process but the analysis was usually limited to the incident plane, later referred to as (OXZ) (where OX is the horizontal shooting direction and OZ the vertical one). In other words, the three-dimensional aspect of the process was simply ignored. This aspect is, however, crucial in the context of aeolian dune formation where the coupling between the downstream transport of grains (i.e., the wind direction) and the transverse one is a key ingredient. The main features of the splash process extracted from 2D analyses of model collision experiments can be summarized as follows [9].

(i) The incident particle loses much more energy in head-on impacts than in grazing collisions. In other words, the effective restitution coefficient $\bar{e}_{2D}$, defined as the ratio of the rebound velocity to the incident one, decreases with increasing impact angle θ_i. Experimental and numerical data [7,9] can be well described by the following law:

$$\bar{e}_{2D} = A_{2D} - B_{2D} \sin \theta_i, \tag{1}$$

where A_{2D} and B_{2D} are fit parameters depending essentially on the material properties of the particles. The overbar should be understood as an ensemble average over several collision experiments achieved in similar conditions.

(ii) The mean number of ejected particles $\bar{n}_{ej}$ increases both with increasing impact velocity V_i and impact angle θ_i, as follows:

$$\bar{n}_{ej} = n_0(1 - \bar{e}_{2D}^2)(V_i/\zeta\sqrt{gd} - 1). \tag{2}$$

The quantities n_0 and ζ are fit parameters, d is the bead diameter, and g the gravity field.

(iii) The sum of the kinetic energy E_{2D} of the splashed beads is proportional to the energy communicated to the granular packing:

$$E_{2D} = r_{2D}(1 - \bar{e}_{2D}^2)E_i, \tag{3}$$

where E_i is the kinetic energy of the incident particle. The quantity r_{2D} characterizes the dissipation within the packing and is on the order of a few percent. Its precise value depends on the material properties of the particles of the packing.

In the present paper, we focus on the 3D aspect of the splash process through a model collision experiment. We performed a set of new collision experiments that were recorded by means of two fast video cameras. Image processing combined with a sophisticated algorithm of trajectory reconstruction allows us to extract the 3D movement of the splashed particles.

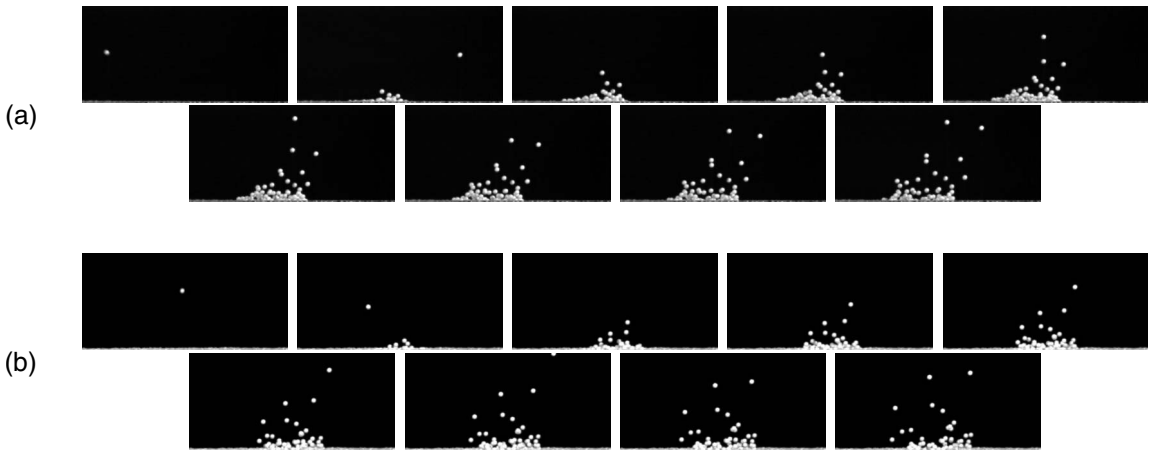

FIG. 1. Sequences of images taken from both cameras: (a) incident plane and (b) transverse plane. The two cameras are synchronized and take 1 frame every 2 ms. The time step between two successive images shown in these sequences is 16 ms and the size of the images is 120×240 mm^2.

The paper is organized as follows. In Sec II, we briefly describe the experimental setup while Sec. III provides the main experimental results. Conclusion is presented in Sec. IV.

II. EXPERIMENTAL SETUP AND 3D METHOD OF TRAJECTORIES CONSTRUCTION

The experimental setup was already described in details in a previous paper [9]. We shall therefore present it briefly. It is composed of an air gun allowing to propel onto a granular packing a spherical bead with a well-controlled velocity and impact angle. The packing is built by placing randomly spherical particles in a square box of dimension $42 \times 42 \times 23$ cm^3 (the solid volume fraction is on the order of 0.6). The impacting particle and the particles of the packing are identical: these are spherical beads of diameter $d=6$ mm. Two different types of beads were used: PVC particles of mass $m=0.2$ g and polypropylene (PP) particles of mass $m=0.1$ g. The restitution coefficient ε in a head-on binary collision is similar for both particle types. For a relative impact velocity of few meters per second, we found $\varepsilon \approx 0.9$.

The novelty lies in the use of two synchronized fast video cameras to visualize the collision process (see Fig. 1). This allows a complete reconstruction of the 3D trajectories of the splashed particles. The optical axis of the first camera was placed perpendicular to the shooting plane, while the second is at the opposite of the shooting direction (see Fig. 2). In other words, we get what happens in the shooting plane (OXZ) from camera 1 and what occurs in the transverse plane (OYZ) from camera 2. The sequence of images from both cameras were analyzed via image processing in order to extract the successive positions of the splashed particles, and an algorithm was developed for the reconstruction of the trajectories of the particles in the 3D space (see Fig. 3). The difficulty of this reconstruction comes from the fact that all particles are identical and some particles can be hidden by other ones during a significant time compared with the duration of their ballistic flight. However, thanks to the two camera views, it is possible to circumvent this last difficulty: particles that are hidden in a given plane are in general apparent in the other plane. The algorithm of trajectory reconstruction then operates using at the same time information coming from both planes. This 3D reconstruction algorithm provides in principle a much better result than a simple 2D reconstruction using a single camera.

At this stage, we should emphasize that it is not possible to detect the low-energy splashed particles, that is, those that hardly detach from the granular bed. As explained in Ref. [9], we introduced a velocity cutoff to define the particles which are considered as ejected particles. Particles that do not reach an altitude greater than a grain diameter are not considered in the analysis. In other words, we disregarded splashed particles having ejection velocities smaller than $\sqrt{2gd}$. We may legitimately wonder whether the experimental results are sensitive on the chosen value of the velocity cut-

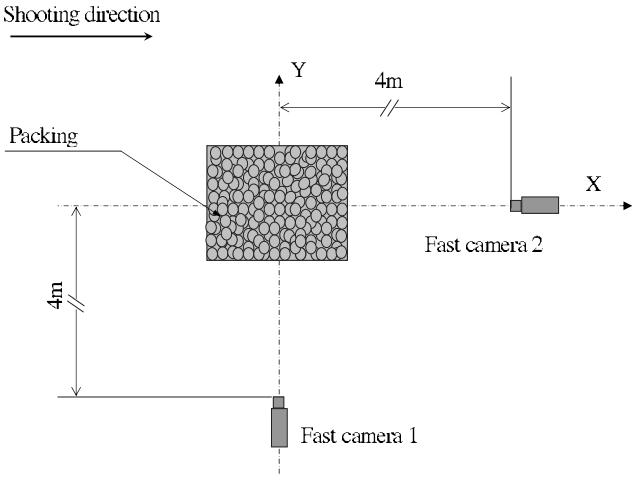

FIG. 2. Top view of the experimental setup. The projectile is propelled from left to right along the (OX) direction and impacts the granular packing at its center. One camera is displayed perpendicularly to the incident plane and the other is at the opposite of the shooting direction. Both cameras are placed at the same distance from the center of the granular packing.

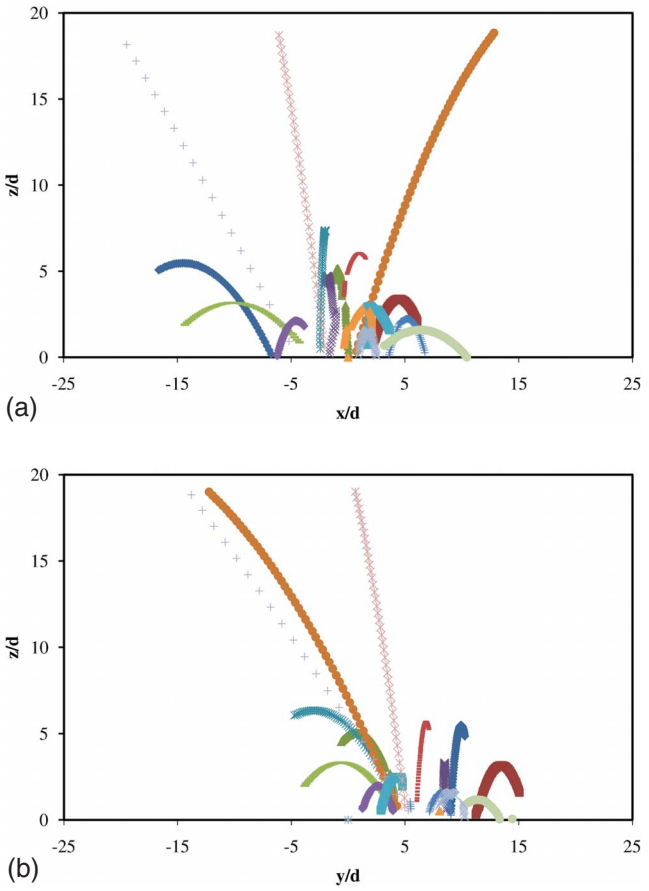

FIG. 3. (Color online) Example of reconstruction of trajectories: (a) incident plane, (b) transverse plane. Note that some trajectories are truncated due to the limitation of the recording duration of the cameras.

off. We showed by means of a discrete model developed in Ref. [13] that the low-energy splashed particles have a negligible contribution in terms of energy. In contrast, the mean number of ejected grains depends most certainly on the velocity cutoff.

III. EXPERIMENTAL RESULTS

We made four sets of collision experiments using PVC particles corresponding to different impact angles ($\theta_i = 10°, 40°, 60°, 90°$) with various impact speeds ranging from $74\sqrt{gd}$ to $161\sqrt{gd}$ (i.e., 18 m/s $< V_i <$ 39 m/s) (see Table I (a)). We also performed an additional series of collisions using PP particles at an impact angle $\theta_i = 10°$ [see Table I (b)].

A. Rebound

A typical collision produces a high-energy particle (that is the rebound particle) and several low-energy particles [1,6,9]. We first focus on the features of the rebound particle when varying the incident speed and impact angle. We define two angles characterizing the rebound (see Fig 4): the rebound angle θ_r measuring the angle between the rebound direction and the horizontal plane, and the azimuthal angle

TABLE I. Experimental impact parameters used for the 3D investigation: (a) Experiments using PVC particles and (b) those using polypropylene particles. For each set of parameters, about 100 collision experiments were achieved.

(a)

	V_i (m/s)				
	18	23	26	29	39
	$\mathrm{Fr} = V_i/\sqrt{gd}$				
θ_i	74	95	107	120	161
10°	×	×	×	×	×
40°	×				×
60°			×		
90°			×		

(b)

	V_i (m/s)	
	26	93
	$\mathrm{Fr} = V_i/\sqrt{gd}$	
θ_i	107	383
10°	×	×

φ_r representing the deviation of the rebound direction from the incident plane. The angle θ_r is restricted to vary between 0 and 90°, while φ_r can vary between −180° and +180° ($\varphi_r = 0$ corresponds to the shooting direction). The rebound angle $\theta_{r,2D}$ measured in the 2D analysis [9] corresponds to the angle between the projection of the rebound direction onto the incident plane and the horizontal shooting direction (OX). One can note that the actual rebound angle θ_r is linked to the 2D rebound angle by the following relation:

$$\tan \theta_r = \cos \varphi_r \tan \theta_{r,2D}. \tag{4}$$

As a consequence, the 2D rebound angle is systematically greater than the actual rebound angle.

As a first result, we did not notice any change of the rebound properties when using PVC particles or PP particles which differ only by their mass. We will therefore present in this subsection only the results obtained using PVC particles. We found, as in the 2D analysis [9], that the mean 3D re-

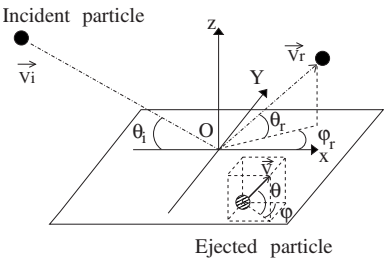

FIG. 4. Definition of the rebound angles (θ_r and φ_r) and ejection angles (θ and φ). θ_r is the angle between the horizontal plane and the rebound direction, whereas φ_r is the angle between the OX axis and the projection of the rebound direction onto the horizontal plane XY. The angles θ and φ characterize similarly the ejection direction of the splashed particles.

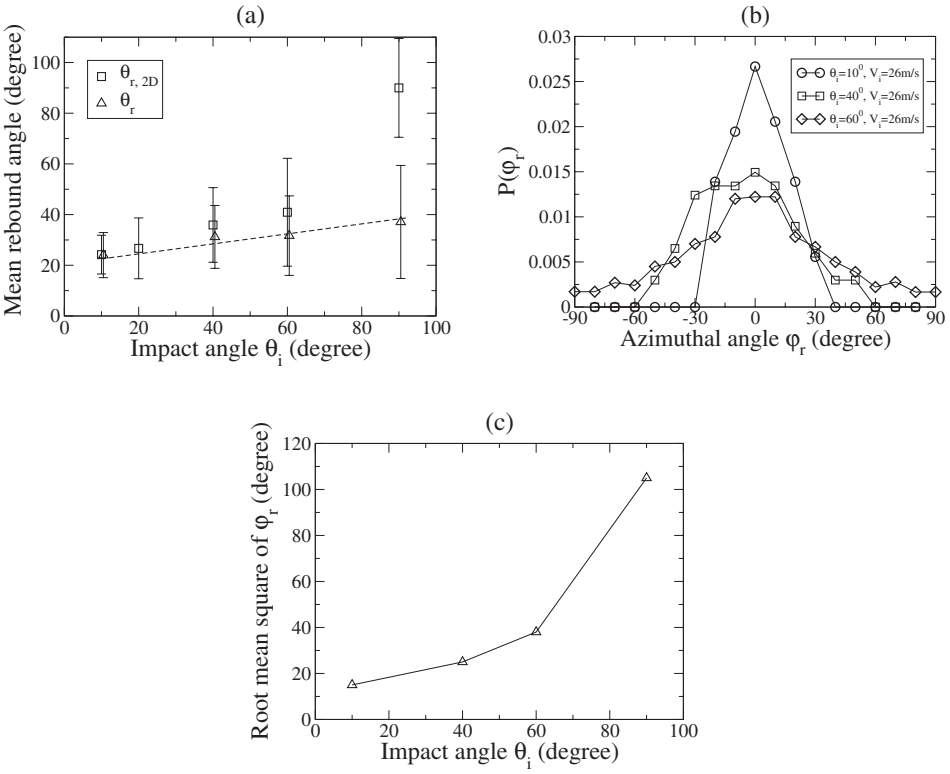

FIG. 5. (a) Variation of the mean actual rebound angle θ_r and the mean 2D angle $\theta_{r,2D}$ as a function of the impact angle for an incident speed $V_i \approx 26$ m/s (except for the experiment performed at $\theta_i = 40°$ for which the impact speed was $V_i \approx 18$ m/s). (b) Distribution of the azimuthal angle for different impact angles. (c) Variation of the root mean square σ_{φ_r} of the azimuthal angle φ_r as a function of the impact angle θ_i.

bound angle was insensitive to variation of the impact velocity but strongly dependent on the incident angle. We plotted, in Fig. 5(a), the mean actual rebound angle $\bar{\theta}_r$ and the corresponding 2D rebound angle $\bar{\theta}_{r,2D}$ as a function of the impact angle. Both rebound angles exhibit the same generic trend: they increase with increasing impact angle but at different rates. However, in contrast to the 2D rebound angle, the 3D rebound angle exhibits a clear linear behavior with the impact angle:

$$\bar{\theta}_r = \theta_0 + \chi \theta_i, \tag{5}$$

with $\theta_0 \approx 20°$ and $\chi \approx 0.19$. Moreover, the difference between 2D and 3D rebound angles increases with increasing impact angle. For an impact angle $\theta_i = 10°$, the relative difference is less than 2%, whereas it is on the order of 30% for $\theta_i = 60°$.

This difference between both rebound angles is due to the deviation of the rebound particle from the incident plane, which is measured by the azimuthal angle φ_r. We displayed in Fig. 5(b) the distributions of the azimuthal angle for different impact angles. Due to symmetry, the mean value of the azimuthal angle is reduced to zero. The width of the distribution is found to increase with increasing impact angle [see Fig. 5(c)]. For normal impacts, the azimuthal angle is expected to be uniformly distributed between $-\pi$ and $+\pi$.

The features of the distribution of the azimuthal angle allow to explain simply the differences observed between 2D and 3D data. As seen previously, geometry tells us that the actual rebound angle θ_r is linked to the 2D rebound angle via the azimuthal angle [see Eq. (4)]. It turns out that if the distribution of the azimuth angle has a finite width, the mean actual rebound angle is systematically smaller than the mean 2D rebound angle. Furthermore, the larger is the distribution width, the greater is the difference between the mean 2D and 3D rebound angle.

To complete the analysis of the rebound, we also calculated the mean restitution coefficient $\bar{e}$, defined as $e = V_r / V_i$, where V_i is the incident velocity and V_r the norm of the rebound velocity ($V_r = \sqrt{V_{rx}^2 + V_{ry}^2 + V_{rz}^2}$). As established in the 2D analysis [7,9], the effective restitution coefficient was found to be independent of the incident speed in the range investigated so far (i.e., $74\sqrt{gd} < V_i < 161\sqrt{gd}$) but extremely sensitive to change of impact angles. Figure 6 shows the evolution of $\bar{e}$ as a function of the impact angle and the corresponding 2D restitution coefficient $\bar{e}_{2D}$ calculated from the 2D rebound velocity V_r^{2D} ($V_r^{2D} = \sqrt{V_{rx}^2 + V_{rz}^2}$). We can see that both restitution coefficients decrease with increasing impact angle and that $\bar{e}$ is systematically greater than $\bar{e}_{2D}$, as

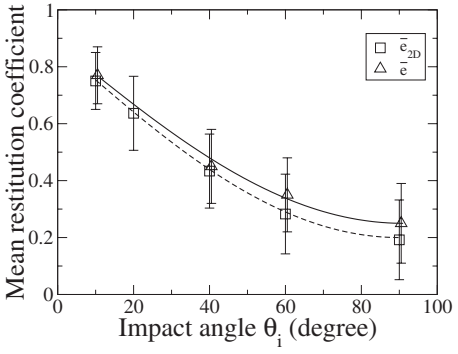

FIG. 6. Mean restitution coefficient $\bar{e}$ and $\bar{e}_{2D}$ versus θ_i. The lines correspond to fits of the form $A - B \sin \theta_i$ ($A = 0.87$ and $B = 0.62$, whereas $A_{2D} = 0.87$ and $B_{2D} = 0.67$).

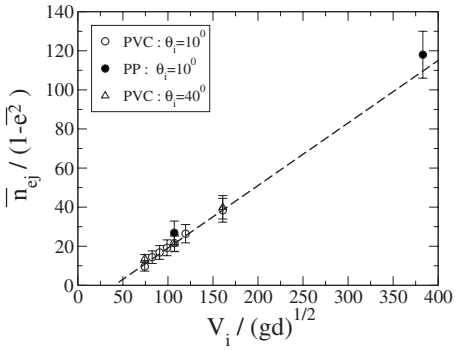

FIG. 7. Mean number of ejected particles renormalized by $(1-\bar{e}^2)$ versus the impact velocity for various impact angles.

expected. Both sets of data can well be approximated by a linear function of sin θ_i [see Eq. (1) for the 2D case]:

$$e = A - B \sin \theta_i \tag{6}$$

with $A = A_{2D} \approx 0.87$, $B_{2D} \approx 0.67$, and $B \approx 0.62$. The difference between $\bar{e}$ and $\bar{e}_{2D}$ increases with increasing impact angle,

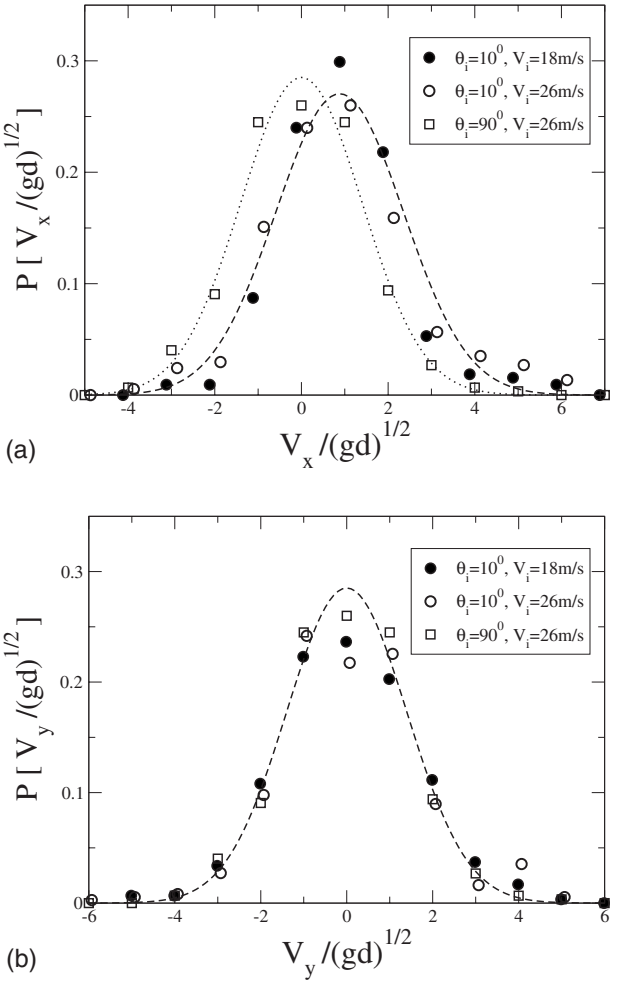

FIG. 8. Distribution of the horizontal ejection speed V_x (a) and V_y (b) for various impact angles and incident velocities. The dashed lines correspond to the best fits using normal laws. Data were obtained with PVC particles.

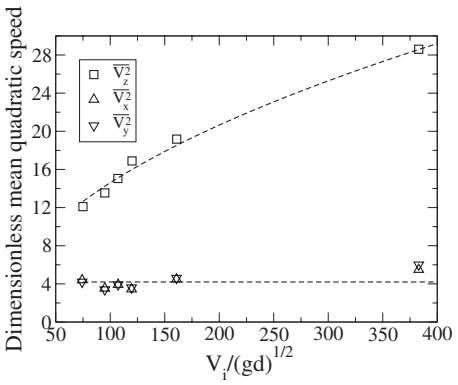

FIG. 9. Dimensionless mean quadratic velocities $\overline{V_x}^2$, $\overline{V_y}^2$, and $\overline{V_y}^2$ versus dimensionless impact velocity at an impact angle $\theta_i = 10°$. The upper dashed curve corresponds to a power law fit giving by Eq. (9).

and becomes significative at large impact angle: for $\theta_i = 10°$, $\Delta\bar{e}/\bar{e} \approx 1\%$, while $\Delta\bar{e}/\bar{e} \approx 10\%$ when $\theta_i = 60°$. This means that the relative contribution of the horizontal transverse component V_{ry} to the 3D rebound velocity becomes more and more important as the impact angle increases.

As a preliminary conclusion, one can safely approximate the rebound angle and the restitution coefficient, respectively, by the 2D rebound angle and the 2D restitution coefficient only in the case of grazing collisions (i.e., for $\theta_i \leqslant 40°$). For impact angles greater than 60°, the relative error is greater than 10%.

B. Features of the splashed particles

We shall now describe the features of the splashed particles and focus on the new information gained from the 3D analysis. As a preliminary result, we did not find any difference about the kinematic properties of the splashed particles when using PVC or PP particles. We will therefore present together the data obtained for PVC and PP particles.

1. Rate of ejected particles

The determination of the number of ejected particles per impact does not require a 3D analysis. However, the 3D

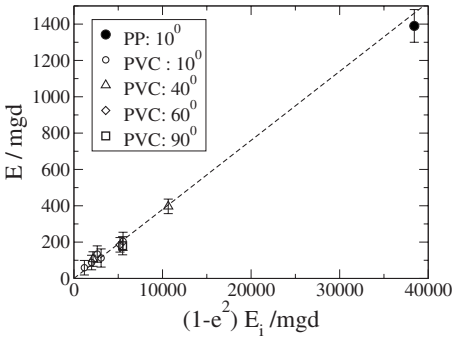

FIG. 10. Sum of the kinetic energy of the splashed particles versus the fraction of energy communicated to the granular bed $(1-\bar{e}^2)E_i$. Note that both quantities were made dimensionless by mgd.

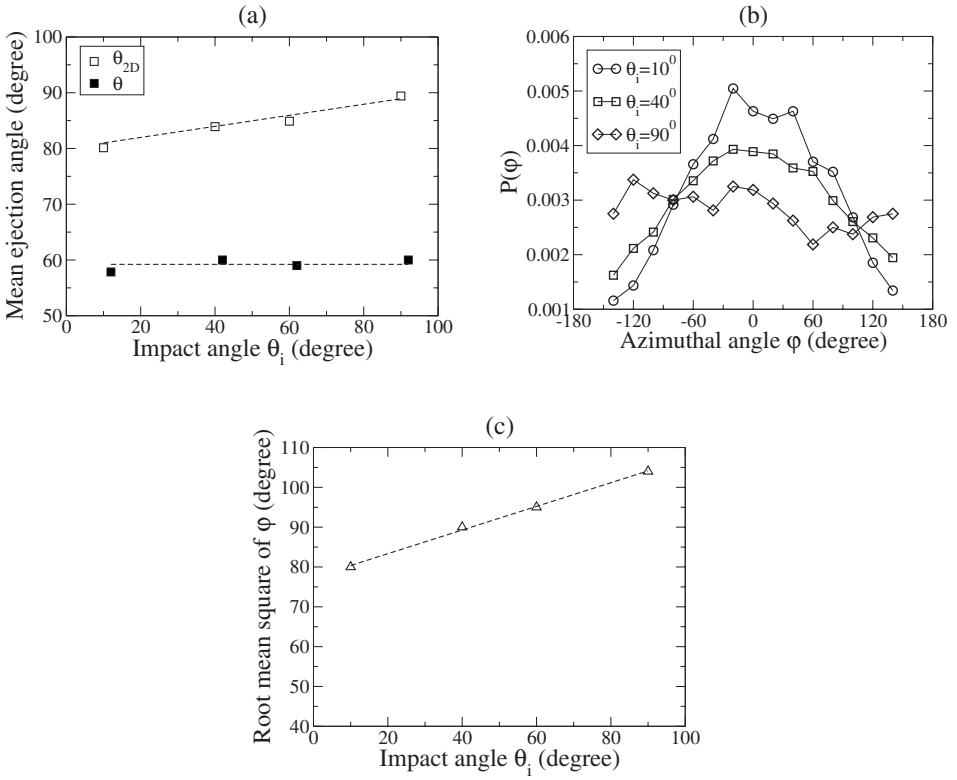

FIG. 11. (a) Mean ejection angle $\bar{\theta}$ versus the impact angle θ_i: (□) 2D ejection angle $\bar{\theta}_{2D}$ and (■) actual ejection angle $\bar{\theta}$. (b) Distributions of the azimuthal angle for different impact angles. (c) Root mean square σ_φ versus impact angle θ_i. These data correspond to collision experiments performed at an impact velocity $V_i=26$ m/s, except for $\theta_i=40°$ where $V_i=18$ m/s. Data were obtained with PVC particles.

treatment provides in principle a better accuracy in the determination of the number of splashed particles, because the use of the two camera views allows us to resolve splashed grains that are not apparent in the incident plane.

The 3D analysis confirms the 2D analysis [9], that is, the mean number of the splashed particles per impact is a linear function of the incident speed (see Fig. 7):

$$\bar{n}_{ej} \approx n_0(1-\bar{e}^2)[V_i/\zeta\sqrt{gd}-1]. \tag{7}$$

with $n_0 \approx 13$ and $\zeta \approx 40$. Further remarks follow. First, the variation of the mean number of splashed grains with the impact angle is found to scale as the fraction of incident energy transferred to the packing $(1-\bar{e}^2)$. In the 2D analysis, we found that for a given impact velocity $\bar{n}_{ej} \sim (1-\bar{e}_{2D}^2)$ [see Eq. (2)]. We may therefore wonder why the scaling obtained in 2D still holds in 3D, considering that we have just seen that $\bar{e}$ and $\bar{e}_{2D}$ differ significantly at large impact angle. This is so, because at large impact angles $\bar{e}$ and $\bar{e}_{2D}$ are much smaller than unity such that $(1-\bar{e}^2) \approx (1-\bar{e}_{2D}^2)$ with a relative error smaller than a few percent. Second, we confirmed here the linearity of $\bar{n}_{ej}$ with the impact velocity by performing a experiment at a much higher impact velocity $(V_i=383\sqrt{gd})$ using light PP particles.

2. Ejection velocity

The 3D analysis allowed us to characterize the three components of the ejection velocity of the splashed grains. The features of the vertical ejection speed V_z were extensively described in Ref. [9]. We recall here only the salient features. The probability distribution of V_z can be well approximated by a log-normal law. It was shown that it is invariant with respect to impact angle changes but slightly sensitive to variations of the impact speed. In particular, the variation of the mean vertical ejection speed (the mean quadratic vertical speed) with the impact speed, can be well approximated by

$$\overline{V_z}/\sqrt{gd} \approx 1.06(V_i/\sqrt{gd})^{1/4}, \tag{8}$$

$$\overline{V_z^2}/\sqrt{gd} \approx 1.46(V_i/\sqrt{gd})^{1/2}. \tag{9}$$

The distribution of the horizontal recoil speeds V_x and V_y for various impact speeds and angles are displayed in Fig. 8. Both distributions are symmetrical and can be approximated by normal laws. The only marked difference is that the distribution for V_x is off-centered and slightly shifted towards positive values. The distributions for V_x and V_y are both hardly sensitive to changes of incident speed and impact angle. As a consequence, the mean quadratic velocities $\overline{V_x}^2$ and $\overline{V_y}^2$ are independent of both impact speed and impact angle (see Fig. 9). Moreover, they have the same order of magnitude

$$\overline{V_x^2} \approx \overline{V_y^2} \approx 4gd. \tag{10}$$

This result indicates that the splashed particles have lost the memory of the incident direction; the packing acts as a diffusive medium with respect to the energy propagation. Finally, we can note that the mean horizontal quadratic velocities are always much smaller than the mean vertical quadratic velocity (see Fig. 9): $\overline{V_x^2} \approx \overline{V_y^2} \leqslant \overline{V_z^2}/3$.

3. Energy balance

We computed from our data the sum of the kinetic energy of the splashed particles $E=m\bar{n}_{ej}\overline{V^2}/2$. We demonstrated (see Fig. 10) that E is a linear function of the fraction of the

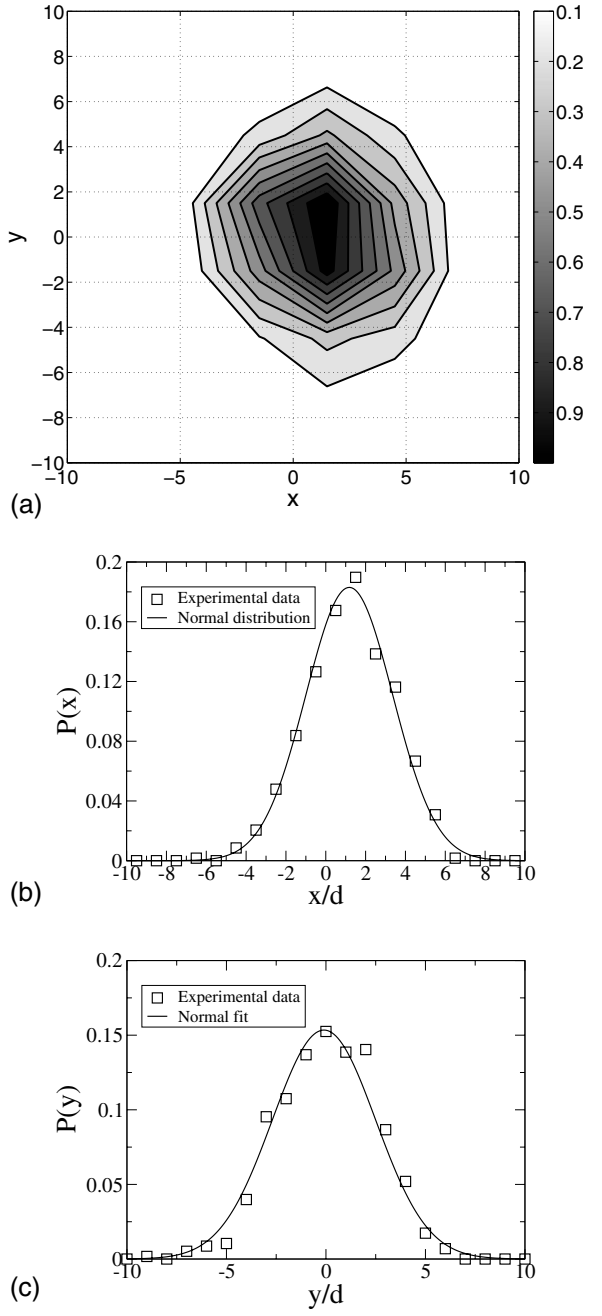

FIG. 12. (a) Typical bivariate distribution $P(x,y)$ of the ejection position of the splashed beads, and corresponding distribution $P(x)$ (b) and $P(y)$ (c). [Note that $P(x)=\int_{-\infty}^{\infty}dyP(x,y)$ and $P(y)=\int_{-\infty}^{\infty}dxP(x,y)$]. $\theta_i=40°$ and $V_i=18$ m/s. The amplitude of $P(x,y)$ is encoded by a gradation in gray levels separated by isoprobability lines with a step $\delta P=0.1P_{\max}$. Data were obtained with PVC particles.

energy communicated to the granular packing $E\approx r(1-\bar{e}^2)E_i$, where E_i is the kinetic energy of the incident particle and r is a constant parameter ($r\approx 0.040$). The same trend was found in the previous 2D analysis [9], but with a smaller coefficient ($r_{2D}\approx 0.038$). It is important to note that r is independent of the mass m of the particles since the same scaling is found for the light PP particles (see Fig. 10). One expects that r depends only on the restitution coefficient ε in a binary collision [13].

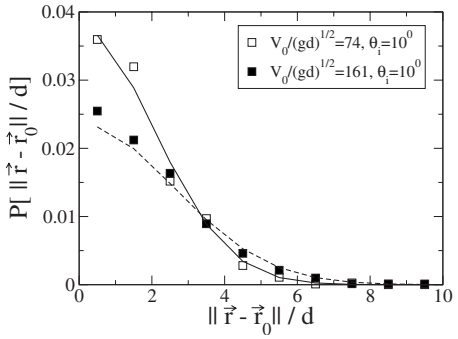

FIG. 13. Distribution $P(\|\vec{r}-\vec{r}_0\|)$ of the ejection location for different impact velocities at an impact angle $\theta_i=10°$. The vector $\vec{r}=x\vec{e}_x+y\vec{e}_y$ denotes the ejection location and $\vec{r}_0$ the position of the peak of the distribution. Continuous lines correspond to normal laws of the form $P(\|\vec{r}-\vec{r}_0\|)=(1/2\pi\sigma_r^2)\exp[-(\vec{r}-\vec{r}_0)^2/2\sigma_r^2]$. Data were obtained with PVC particles.

4. Ejection angle

As for the rebound, the ejection direction of the splashed particles is characterized by two angles, the ejection angle θ, or latitude (measuring the angle with respect to the horizontal plane), and the azimuthal angle φ (see Fig. 4).

We recall that in the 2D analysis of the ejection process, the mean ejection angle measured in the incident plane $\bar{\theta}_{2D}$ was found to be insensitive to variations of the incident speed but increased slightly with increasing impact angle [9,11,14]. The 3D analysis reveals that the mean ejection angle $\bar{\theta}$ is surprisingly independent on both the incident speed and impact angle [see Fig. 11(a)]. The latter is equal to 60°. Once again, the ejection angle keeps no memory of the incident direction.

The difference observed between the mean 2D and 3D ejection angles can be inferred, as for the rebound angle, from the features of the distribution of the azimuthal angle. In Fig. 11(b) the distributions of the azimuthal angle φ are displayed for different impact angles. The width of the distributions is relatively large, and is found to increase only slightly with increasing impact angle [see Fig. 11(c)]. The distribution of the azimuthal angle for normal impacts is expected to be uniform due to symmetry. However, it is surprising to note that for grazing impacts (i.e., $\theta_i=10°$), the distribution width is still relatively large ($\sigma_\varphi\approx 80°$).

As seen previously for the rebound angle [see Eq. (4)], the 2D and 3D ejection angles obey the following relation: $\tan\theta\approx\cos\varphi\tan\theta_{2D}$. The difference between 2D and 3D ejection angles is due to the fact that the azimuthal angle is distributed around zero with a finite dispersion, such that the mean 3D ejection angle is systematically smaller that the mean 2D ejection angle. Moreover, the difference is enhanced for large distribution width of the azimuthal angle.

5. Ejection location

At last, we shall discuss on the ejection location of the splashed beads. In Fig. 12, we show a typical bivariate dis-

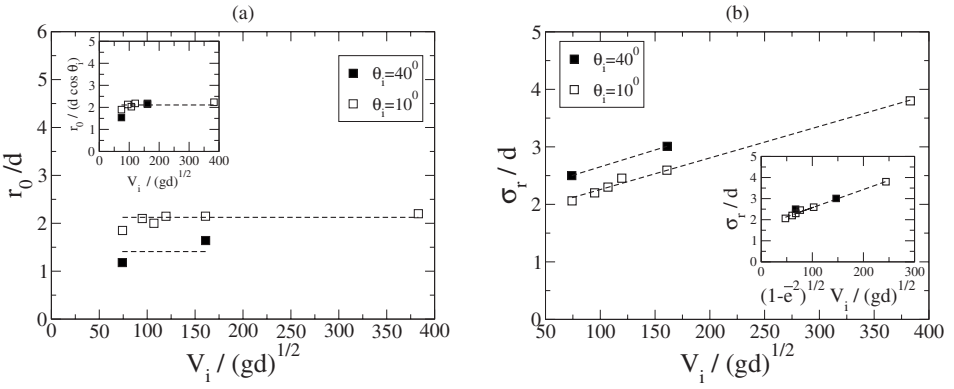

FIG. 14. (a) Evolution of the peak position r_0 as function of the impact velocity. Inset: Same data with r_0 rescaled by $\cos\theta_i$. (b) Evolution of the distribution width as a function the impact velocity. Inset: Same data plotted as a function $\sqrt{1-\bar{e}^2}V_i/\sqrt{gd}$. Data were obtained with PVC particles.

tribution $P(x,y)$ for the ejection location of the splashed particles. Note that the impact point is taken as the origin of the coordinate system. One can note first that the region concerned by the ejection process is rather isotropic: no direction is preferred. Secondly, the distribution is off-centered and shifted towards the shooting direction. Lastly, the distribution $P(x)$ and $P(y)$ can be well approximated by a normal law [see Fig. 12(b) and 12(c)].

We found in addition that the x and y coordinates of the ejection location can be safely considered as uncorrelated. The correlation coefficient $\rho(x,y)$ [defined as $\rho(x,y)=(\overline{xy}-\overline{x}\,\overline{y})/\sigma_x\sigma_y$] is always smaller than 0.2. As a consequence, the distribution of the ejection location can be approximated by the product of two independent univariate normal distributions with identical variances ($\sigma_x=\sigma_y\equiv\sigma$). Figure 13 shows the distribution $P(\|\vec{r}-\vec{r}_0\|)$ for different impact speeds at an impact angle $\theta_i=10°$. The vector $\vec{r}=x\vec{e}_x+y\vec{e}_y$ denotes the ejection location and $\vec{r}_0$ the position of the distribution peak. These distributions are well fitted by normal laws $P(\|\vec{r}-\vec{r}_0\|)=(1/2\pi\sigma^2)\exp[-(\vec{r}-\vec{r}_0)^2/2\sigma^2]$. The position $\vec{r}_0=r_0\vec{e}_x$ of the distribution peak is found relatively close to the impact point, from one to two grain diameters [see Fig. 14(a)]. The quantity r_0 clearly increases with decreasing impact angle and does not vary significantly with increasing impact velocity. Our data can be approximated by the following scaling law:

$$r_0 \approx 2d\cos\theta_i. \tag{11}$$

The dispersion width of these distributions is found to increase both with increasing impact speed and impact angle [see Fig. 14(b)]. Its amplitude is strongly correlated to the incident energy transferred to the packing $(1-\bar{e}^2)E_i$, which is an increasing function of the impact speed and incident angle. We indeed found that the variation of the distribution width σ_r with the impact angle and impact velocity can be well described by the following law:

$$\frac{\sigma_r}{d} \approx 1.7 + 0.0086\frac{\sqrt{1-\bar{e}^2}V_i}{\sqrt{gd}} \tag{12}$$

IV. CONCLUSION

We performed a 3D analysis of the collision process between an incident bead onto a packing composed of particles identical to the incident one. We obtained a rather complete description of the splash process, which may be useful for the development of future aeolian sand transport models incorporating the 3D aspect of the process. Furthermore, the data provided here may also serve to test models for the propagation of energy in a granular packing [13,15].

The 3D analysis performed here provided new information inaccessible to a 2D treatment. The most salient features can be summarized as follows. (i) The angle of rebound was found independent of the impact speed and weakly sensitive to changes of the impact angle. It varies from 25° to 35° when increasing the impact angle from 10° to 90°. In addition, the incident bead, after the impact, deviates from the incident plane, and the deviation increases with increasing impact angle. (ii) The 3D analysis also revealed that the features of the splashed particles (such as the azimuthal ejection angle, the ejection location,…) are isotropic with respect to the horizontal directions. In other words, the splashed particles lost the memory of the original impact direction. This results suggests that the bead packing plays the role of a perfect diffusive medium with respect to the energy propagation [13]. Furthermore, the fact that the ejection angle of the splashed particles is invariant (and equal to 60°) reinforces this idea. (iii) Lastly, we demonstrated that the dispersion width of the ejection location is strongly correlated to the incident energy transferred to the packing.

[1] R. A. Bagnold, *The Physics of Blown Sand and Desert Dunes* (Chapmann and Hall, Methuen, London, 1941).
[2] B. R. White and J. C. Schulz, J. Fluid Mech. **81**, 497 (1977).
[3] P. Napalnis, J. C. Hunt, and C. F. Barrett, J. Fluid Mech. **251**, 661 (1993).
[4] M. A. Rice, B. B. Willets, and I. K. McEwan, Sedimentology **43**, 21 (1996).
[5] D. Wang, Y. Wang, B. Yang, and W. Zhang, Sedimentology **55**, 461 (2008).
[6] S. Mitha, M. Q. Tran, B. T. Werner, and P. K. Haff, Acta Mech.

63, 267 (1986).
[7] B. T. Werner, J. Geol. **98**, 1 (1990).
[8] F. Rioual, A. Valance, and D. Bideau, Phys. Rev. E **62**, 2450 (2000).
[9] D. Beladjine, M. Ammi, L. Oger, and A. Valance, Phys. Rev. E **75**, 061305 (2007).
[10] B. T. Werner and P. K. Haff, Sedimentology **35**, 189 (1988).
[11] R. S. Anderson, M. Sorensen, and B. B. Willets, Acta Mech. Suppl. **1**, 1 (1991).
[12] L. Oger, M. Ammi, A. Valance, and D. Beladjine, Eur. Phys. J. E **17**, 467 (2005).
[13] J. Crassous, D. Beladjine, and A. Valance, Phys. Rev. Lett. **99**, 248001 (2007).
[14] B. B. Willets and M. A. Rice, Acta Mech. **63**, 255 (1986).
[15] J. Crassous and A. Valance (unpublished).